Traveling waves in rotating Rayleigh-Bénard convection

Wooyoung Choi,[1,2,*] Dilip Prasad,[1,2,†] Roberto Camassa,[1,2] and Robert E. Ecke[2,3]
[1]*Theoretical Division, Los Alamos National Laboratory, Los Alamos, New Mexico 87545, USA*
[2]*Center for Nonlinear Studies, Los Alamos National Laboratory, Los Alamos, New Mexico 87545, USA*
[3]*Materials Science and Technology Division, Los Alamos National Laboratory, Los Alamos, New Mexico 87545, USA*
(Received 19 September 2003; published 12 May 2004)

A combined analytical, numerical, and experimental study of the traveling-wave wall mode in rotating Rayleigh-Bénard convection is presented. No-slip top and bottom boundary conditions are used for the numerical computation of the linear stability, and the coefficients of the linear complex Ginzburg-Landau equation are then computed for various rotation rates. Numerical results for the no-slip boundary conditions are compared with free-slip calculations and with experimental data, and detailed comparison is made at a dimensionless rotation rate $\Omega=274$. It is found that the inclusion of the more realistic no-slip boundary conditions for the top and bottom surfaces brings the numerical linear stability analysis into better agreement with the experimental data compared with results using free-slip top/bottom boundary conditions. Some remaining discrepancies may be accounted for by the finite conductivity of the sidewall boundaries.

DOI: 10.1103/PhysRevE.69.056301 PACS number(s): 47.20.Bp, 47.32.−y, 47.54.+r

I. INTRODUCTION

Rayleigh-Bénard convection in the presence of rotation about a vertical axis exhibits many features not seen in convection without rotation. For example, at high rotation rates the first instability of the conductive state is not to a bulk mode as predicted by Chandrasekhar [1] but rather to a traveling-wave state localized near sidewall boundaries. The first evidence for this mode can be seen in heat transport measurements [2,3]; a partial explanation [4] was based on linear stability calculations [5] which predicted a stationary azimuthally periodic wall mode. Flow visualization of rotating convection in a cylindrical convection cell with radius-to-height ratio $\Gamma=1$ revealed, however, that the wall mode was a traveling wave [6,7]. The traveling-wave form of the wall mode follows quite generally from the broken left-right symmetry in rotating systems [8].

Linear stability calculations in bounded cylindrical geometry of $\Gamma=1$ by Goldstein *et al.* (GMNK) [9] and for an infinite slab of $\Gamma=\infty$ by Kuo and Cross (KC) [10] and Hermann and Busse (HB) [11] also demonstrated the traveling nature of the instability and provided numerical estimates for the parameters at the onset of the instability. The infinite slab calculations used rigid sidewall boundaries but free-slip boundary conditions on the top and bottom boundaries, whereas the bounded geometry calculations investigated both free-slip and rigid top/bottom boundary conditions. Recently, agreement between linear stability calculations including rigid top-plate conditions for a straight wall at $\Omega=274$ [12] by Plaut (P) and a direct numerical simulation of the wall mode in a curved geometry [13] by Scheel, Paul, Cross, and Fisher (SPCF), also at $\Omega=274$, implied that wall curvature does not play a large role in deviations seen in comparison between experiment and linear stability calculations.

Further experimental work by Ning and Ecke (NE) [14] in a convection cell with a larger aspect ratio, $\Gamma=2.5$, showed that the traveling-wave state was well-described by the complex Ginzburg-Landau (CGL) equation (for a review of the application of amplitude equations to problems in pattern formation, see Ref. [15]). The experimentally determined coefficients compared reasonably well with the theoretical predictions of KC for free-slip top/bottom boundary conditions. Because the CGL equation should apply best to laterally large systems, a set of experiments with $\Gamma=5$ was recently performed by Liu and Ecke (LE) [16,17]. They determined the coefficients of the CGL equation as well as some higher-order corrections, mapped out the Eckhaus-Benjamin-Feir [18–21] stability boundary and measured properties of phase diffusion in the stable wave-number band.

These recent experiments for larger aspect ratios provided more detailed information regarding the traveling-wave state in convection under rotation, which prompted us to reexamine the linear analysis for an infinite slab with the more realistic boundary conditions. Before presenting our results, we describe briefly the physical system. Details of the experimental apparatus can be found elsewhere [17].

Rayleigh-Bénard convection with rotation about a vertical axis [1] is described by the following three-dimensionless parameters: Ra, Ω, and Pr. The Rayleigh number, a measure of the thermal forcing of the system, is defined by $Ra=g\alpha d^3\Delta\theta/\nu\kappa$, where g is the acceleration of gravity, α is the thermal expansion coefficient, $\Delta\theta$ is the temperature difference across a fluid layer of height d, ν is the kinematic viscosity, and κ is the fluid thermal diffusivity. The strength of the Coriolis force resulting from rotation about a vertical axis at angular rotation frequency Ω_D is measured by the dimensionless rotation rate $\Omega=\Omega_D d^2/\nu$. (The Coriolis force is sometimes parametrized by the dimensionless Ekman number which is the inverse of Ω.) The third parameter is the Prandtl number $Pr=\nu/\kappa$ which controls the dominant form

*Present address: Department of Naval Arch. and Marine Engineering, University of Michigan, Ann Arbor, MI 48019, USA.
†Present address: United Technologies Research Center, East Hartford, CT 06108, USA.

of the nonlinearity in thermal convection. The centrifugal force is not important for these experiments in which the ratio of the centrifugal acceleration $\Omega_D^2 R$, where R is the cell radius, to the gravitational acceleration g is 0.03 (see, for example, the heat transport curve in Ref. [22]). For fixed Pr, the bifurcation parameter for the convection problem is $\epsilon = Ra/Ra_c - 1$, where $Ra_c(\Omega)$ is the critical Rayleigh number for the onset of convection. Rotation suppresses that onset and, for large Ω, the critical Rayleigh number for the bulk mode Ra_b scales like $\Omega^{4/3}$ [1], whereas Ra_c for the wall mode with insulating sidewall boundaries scales as Ω [10,11]. The geometry also enters the problem and is represented by the aspect ratio Γ which is the radius-to-height ratio for a cylindrical convection cell.

This paper is organized in the following order: After introducing the governing equations with the boundary conditions in Sec. II, the linear stability analysis is carried out analytically for the free-slip boundary condition and numerically for the no-slip boundary condition. Then the linear coefficients of the CGL equations are computed. In Sec. III, we compare our results with experimental data and earlier numerical solutions. Further discussions and conclusion are made in Sec. IV.

II. GOVERNING EQUATIONS

For our experimental setup, the dynamics of the fluid is governed by the incompressible Navier-Stokes equations in the Boussinesq approximation. Adopting Cartesian coordinates centered at the midplane of the cell and on the sidewall, these equations are conveniently written in terms of the vorticity field $\boldsymbol{\omega} = \boldsymbol{\nabla} \times \boldsymbol{u}$, where $\boldsymbol{u}(\boldsymbol{x},t) = (u,v,w)$ is the three-dimensional velocity vector,

$$\boldsymbol{\omega}_t - Pr(\nabla^2 \boldsymbol{\omega} + 2\Omega \boldsymbol{u}_z + \boldsymbol{\nabla} \times \theta \mathbf{k}) = (\boldsymbol{\omega} \cdot \boldsymbol{\nabla})\boldsymbol{u} - (\boldsymbol{u} \cdot \boldsymbol{\nabla})\boldsymbol{\omega}, \tag{1}$$

$$\theta_t - \nabla^2 \theta - Ra\, w = -\boldsymbol{u} \cdot \boldsymbol{\nabla}\, \theta. \tag{2}$$

Here we have nondimensionalized the equations by scaling length by d, time by d^2/κ, temperature $\theta(\boldsymbol{x},t)$ by $\kappa\nu/(\alpha g d^3)$, thereby collecting the three-dimensionless parameters introduced in Sec. I, respectively, Ra, Ω, and Pr. Notice that the temperature θ is measured with respect to the conducting solution $\boldsymbol{u} = \mathbf{0}$, $\theta_c = \Delta\theta(1 - 2z/d)/2$.

For boundary conditions at the sidewall, we impose no slip for velocity $\boldsymbol{u}$ and insulation for temperature θ,

$$\boldsymbol{u} = \mathbf{0}, \quad \theta_y = 0 \quad \text{at } y = 0. \tag{3}$$

The system is assumed to relax to the conducting state far from the sidewall, so that we can take zero boundary conditions at $y = \infty$,

$$\boldsymbol{u} \to \mathbf{0}, \quad \theta \to 0 \quad \text{as } y \to \infty. \tag{4}$$

At the top and bottom surfaces, we consider two different boundary conditions: no-slip boundary condition,

$$\boldsymbol{u} = \mathbf{0}, \quad \theta = 0 \quad \text{at } z = \pm \frac{d}{2}, \tag{5}$$

free-slip boundary condition,

$$u_z = v_z = w = 0, \quad \theta = 0 \quad \text{at } z = \pm \frac{d}{2}. \tag{6}$$

The free-slip boundary conditions at the top and bottom are unphysical, but analytic solutions are available for this case. These can be used to validate our algorithm for solving the no-slip case which can only be treated numerically. Further simplification can be achieved by introducing the velocity vector potential

$$\begin{aligned} \boldsymbol{u} &= \boldsymbol{\nabla} \times (\chi \mathbf{i} + \phi \mathbf{j} + \psi \mathbf{k}) \\ &= (\psi_y - \phi_z)\mathbf{i} + (-\psi_x + \chi_z)\mathbf{j} + (\phi_x - \chi_y)\mathbf{k}, \end{aligned} \tag{7}$$

where the components $\chi(y,z,t)$, $\phi(x,y,z,t)$, and $\psi(x,y,z,t)$ are the new unknowns to be determined and $(\mathbf{i},\mathbf{j},\mathbf{k})$ are the unit vectors in the (x,y,z) directions. The velocity field generated by Eq. (7) is consistent with either free-slip or no-slip boundary conditions on $\boldsymbol{u}$ (which eliminate the need of a scalar potential). The x component of the vector potential χ (corresponding to the Stokes streamfunction for axisymmetric flows about the vertical axis in cylindrical geometry) is not necessary for *linear* traveling waves, since it would correspond to the zero-wave-number mode, and in the following analysis we assume $\chi = 0$. The vorticity is then given, in terms of the vector potential, by

$$\begin{aligned} \boldsymbol{\omega} = \boldsymbol{\nabla} \times \boldsymbol{u} &= (\phi_{xy} + \psi_{xz})\mathbf{i} + (\psi_{yz} - \phi_{xx} - \phi_{zz})\mathbf{j} \\ &\quad + (\phi_{yz} - \psi_{xx} - \psi_{yy})\mathbf{k}. \end{aligned} \tag{8}$$

A. Amplitude equation

The conducting state, corresponding to the zero solution for Eqs. (1) and (2), becomes unstable for certain values of the parameters. Mathematically, these can be determined through the study of a linear eigenvalue problem. Assuming that the instability manifests itself as small amplitude (appropriate near onset) traveling waves, we can write $\boldsymbol{\Phi} = (\phi, \psi, \theta)^T$ as

$$\boldsymbol{\Phi}(x,y,z,t) = A\boldsymbol{\Phi}_1(y,z)\mathrm{e}^{\mathrm{i}kx + \sigma t} + \text{c.c}, \tag{9}$$

where A is the complex wave amplitude, k is the wave number, and c.c. stands for the complex conjugate. When $\mathrm{Re}[\sigma] > 0 (< 0)$, the system is linearly unstable (stable). The smallness assumption allows us to linearize Eqs. (1) and (2). Taking into account Eq. (9) yields the eigenvalue problem

$$(\sigma \boldsymbol{L}_1 + \boldsymbol{M}_1)\boldsymbol{\Phi}_1 = \mathbf{0}, \tag{10}$$

for operators $\boldsymbol{L}_1$ and $\boldsymbol{M}_1$ which can be read off the left-hand side of Eqs. (1) and (2), with the boundary conditions for the eigenfunction $\boldsymbol{\Phi}_1$ from Eqs. (3) and (6), namely,

$$\phi_1 = \psi_1 = \psi_{1y} = \theta_{1y} = 0 \quad \text{at } y = 0, \tag{11}$$

$$\phi_1 = \psi_1 = \theta_1 = 0 \quad \text{as } y \to \infty, \tag{12}$$

for the no-slip case,

$$\phi_1 = \phi_{1z} = \psi_1 = \theta_1 = 0 \quad \text{at } z = \pm \tfrac{1}{2}, \tag{13}$$

and, for the free-slip case,

$$\phi_1 = \phi_{1zz} = \psi_{1z} = \theta_1 = 0 \quad \text{at } z = \pm \tfrac{1}{2}. \tag{14}$$

As shown earlier [10,11], solutions of Eq. (10) with the free-slip boundary condition (14) are separable and can be found almost entirely by analytic tools. We used these solutions to validate our numerical computations for the case of no-slip boundary condition, where a closed-form solution is not available and a fully two-dimensional eigenvalue problem must be solved. To solve Eq. (10) numerically, we used a pseudospectral method similar to that developed by Marques *et al.* [23]. The semi-infinite domain is truncated at some (large) $y=L$, where we impose the boundary condition for $y=\infty$. The sensitivity on the size L of the computational domain is expected to be very low because the experimentally observed traveling waves are confined in a narrow region close to the wall. The effect of the domain size will be examined in detail later. In both free-slip and no-slip cases, Newton-Raphson can be used to find iteratively the critical wave number k_c and the critical Rayleigh number Ra_c, which is the minimum value of Ra for which $\mathrm{Re}[\sigma]=0$. Then the eigenvalue becomes the wave frequency $\omega_c=\mathrm{Im}[\sigma_c]$, and the corresponding eigenfunction $\mathbf{\Phi}_1$ determines the velocity-temperature field, respectively.

Next, solutions away from the critical value Ra_c can be obtained in the form of a traveling wave solution Eq. (9) which is slowly modulated in space and time by letting the amplitude A vary slowly in x and t,

$$\mathbf{\Phi}_1(x,y,z,t) = A(x,t)\mathbf{\Phi}_1(y,z)\mathrm{e}^{\mathrm{i}(k_c x+\omega_c t)} + \mathrm{c.c}, \tag{15}$$

where ω_c and k_c are the critical wave frequency and wave number.

A multiscale asymptotic expansion with respect to the small parameter $\epsilon \equiv (Ra-Ra_c)/Ra_c \ll 1$ results in the complex Ginzburg-Landau (CGL) equation with periodic boundary conditions for the evolution of the amplitude A [15,17],

$$\tau_0(A_t + c_g A_x) = \epsilon(1+ic_0)A + \xi_0{}^2(1+ic_1)A_{xx} - g_0(1+ic_2)|A|^2 A, \tag{16}$$

where all the coefficients are real, τ_0 is the time scale, ξ_0 is the spatial scale, c_g is the group velocity, ϵ is the linear bifurcation parameter, and g_0 is the nonlinear parameter. The coefficients c_i's control the dependence of the modulation frequency on modulation wave number and on ϵ.

In their experiments, LE [17] measured c_g, τ_0, ξ_0, and c_0-c_1, and showed that the traveling-wave wall mode provides a classic example of a physical nonlinear-wave system with a supercritical bifurcation described by the CGL equation. Thus, a test of how well the theory describes the experiment can be carried out by computing the CGL coefficients. For this purpose, it is in general necessary to expand the solution $\mathbf{\Phi}$ to third order in terms of ϵ and to impose the solvability condition on the higher-order equations. This procedure is standard but a bit laborious and we omit the details; we report the result for the coefficients of the linear terms in the CGL equation in Table II.

For the linear-term coefficients there is an alternative to carrying out the expansion to higher-orders by making use of our numerical solutions for linear stability. After computing σ near the critical Rayleigh number and wave number, we calculate numerically the first- and second-order derivatives of σ with respect to k and Ra at (k_c, Ra_c) to obtain

$$c_g = \mathrm{i}\left.\frac{\partial\sigma}{\partial k}\right|_c, \quad \alpha = -Ra_c\left.\frac{\partial\sigma}{\partial Ra}\right|_c, \quad \beta = \frac{1}{2}\left.\frac{\partial^2\sigma}{\partial k^2}\right|_c, \tag{17}$$

where the subscript c stands for the evaluation at the critical values (k_c, Ra_c). In our computations, a second-order finite difference is used to evaluate Eq. (17) and gives accurate results (see below). The derivatives in Eq. (17) are the coefficients of the linear CGL equation [24] in the form

$$A_t + c_g A_x + \epsilon\alpha A + \beta A_{xx} = 0. \tag{18}$$

Comparing Eq. (18) with Eq. (16), we have

$$\tau_0 = -\frac{1}{\alpha_r}, \quad \xi_0{}^2 = \frac{\beta_r}{\alpha_r}, \quad c_0 = \frac{\alpha_i}{\alpha_r}, \quad c_1 = \frac{\beta_i}{\beta_r}, \tag{19}$$

and the subscripts r and i represent the real and imaginary parts, respectively.

When we choose $A=A_0\exp(\mathrm{i}(qx-st))$, where $q=k-k_c$ and A_0 is a real constant, and substitute this into the CGL equation (16), the real and imaginary parts yield

$$\epsilon = \xi_0{}^2 q^2 + g_0 A_0{}^2, \tag{20}$$

$$s = c_g q - \frac{1}{\tau_0}(c_0\epsilon - c_1\xi_0{}^2 q^2 - c_2 g_0 A_0{}^2). \tag{21}$$

For small amplitude waves ($A_0 \ll 1$), Eq. (20) at the marginal stability boundary gives at leading order $\epsilon_M = \xi_0{}^2 q^2$. Differentiating Eq. (21) with respect to q, we find the group velocity v_g as

$$v_g = c_g + \frac{2c_1\xi_0^2}{\tau_0}q, \tag{22}$$

and, at the critical condition ($q=0$), we recover $v_g = c_g$.

III. NUMERICAL RESULTS AND DISCUSSIONS

For the numerical results described here, we chose $Pr=6.3$ following the experiment of Liu and Ecke [17]. Prior to comparing with experimental data, we validate our numerical solutions. For the free-slip boundary conditions at the top and bottom boundaries, we compare our numerical solutions with those derived analytically [10,11].

As shown in Table I, our numerical solutions for Ra_c and ω_c are accurate for various choices of grid size (Δ) and computational domain size (L). Since we are interested in the wall mode for which all disturbances are concentrated near

TABLE I. Comparison between exact and numerical solutions for the free-slip boundary conditions. For this computation, $\Delta_y=\Delta$, $\Delta_z=\Delta/2$, $\Omega=274$, and Ra_c and ω_c are evaluated at $k_c d=3.968$.

	Exact	$\Delta=1/8$ $L=2$	$\Delta=1/10$ $L=2$	$\Delta=1/8$ $L=3$
Ra_c	19843.8	19841.2	19846.8	19843.9
Error (%)	0	−0.01	0.015	0.005
ω_c	24.213	24.202	24.213	24.212
Error (%)	0	−0.08	0	−0.04

the sidewall boundary, the relatively small computational domain in the y direction appears to work well. Under the limitation of our computational resources, we chose $L=2$ and $\Delta=1/10$ in all of the computations presented hereafter. With this choice, the maximum error in our numerical solutions is less than 3 % for any physical quantities as well as for the coefficients of the CGL equation.

Since no analytic solutions are available for the case of rigid boundary, we tested our code for the no-slip boundary condition by comparing results from the two different methods described above, i.e., we compared the values of linear CGL coefficients obtained by imposing the solvability condition with those obtained by taking finite difference derivatives with respect to the parameters. As shown in Table II,

TABLE II. Comparison of numerical solutions from two different methods for the no-slip boundary condition. For this computation, $\Omega=274$, $Ra_c=19646.97$, $k_c=4.221$, and $\omega_c=22.413$. Method 1: differentiation of σ as shown in Eq. (17). Method 2: solvability condition.

	Method 1	Method 2
c_g	1.918320	1.918320
α_r	−39.807999	−39.807999
α_i	−25.342976	−25.342918
β_r	−1.7404456	−1.7404476
β_i	−0.8259564	−0.8259625

the two results are almost identical which gives confidence in the code's reliability.

For $\Omega=274$, the computed eigenfunctions $\mathbf{\Phi}_1=(\phi,\psi,\theta)$ are presented in Fig. 1. The concentration of all disturbances near the wall boundary at $y=0$ is immediately evident and the use of a finite computational domain is therefore justified. The corresponding streamlines in the (x,z) plane and the (x,y) plane are shown in Fig. 2 and the temperature distribution in the (x,y) plane is shown in Fig. 3.

We now present our numerical results for linear coefficients of the wall mode in rotating convection. We make extensive comparison with existing experimental (NE,LE)

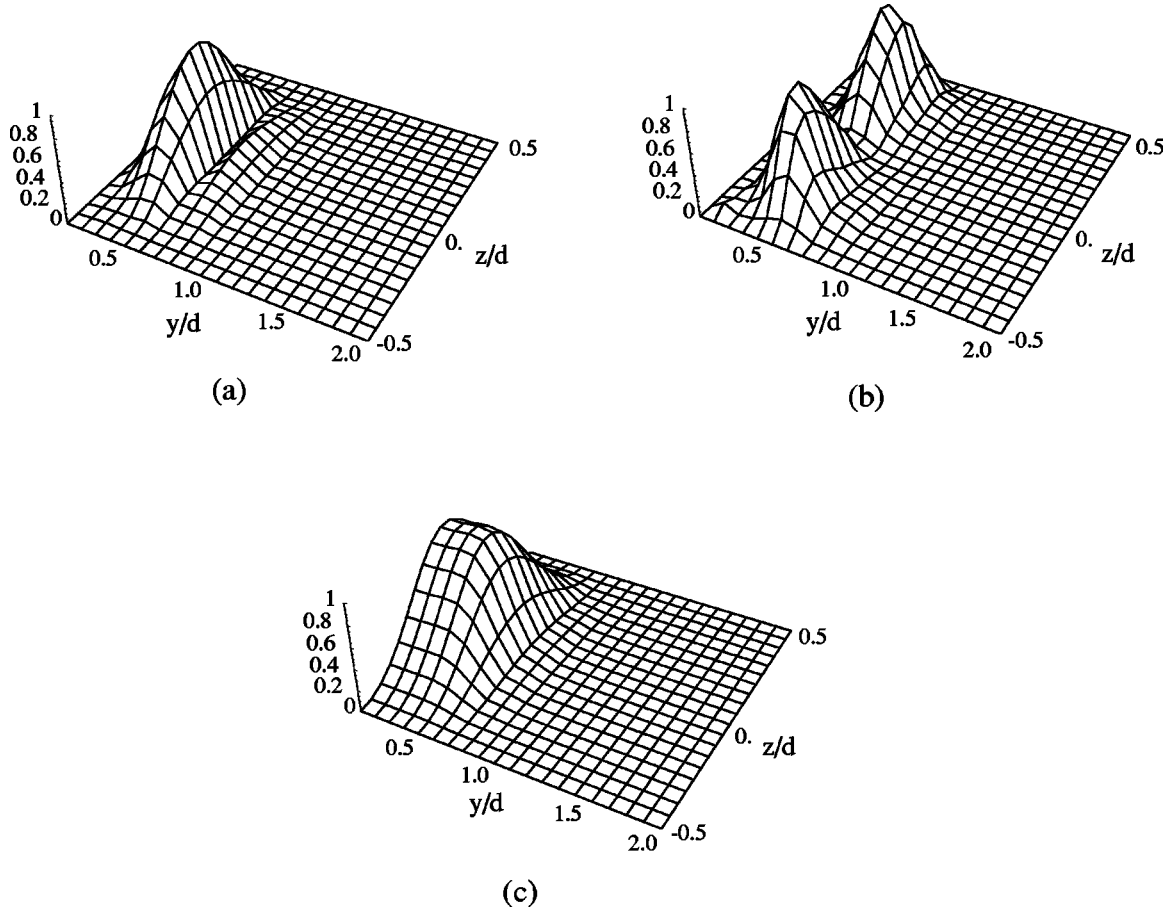

FIG. 1. Eigenfunctions for $Ra=Ra_c$ and $\Omega=274$ with no-slip boundary condition: (*a*) $|\phi|/|\phi|_{\max}$, (*b*) $|\psi|/|\psi|_{\max}$, (*c*) $|\theta|/|\theta|_{\max}$

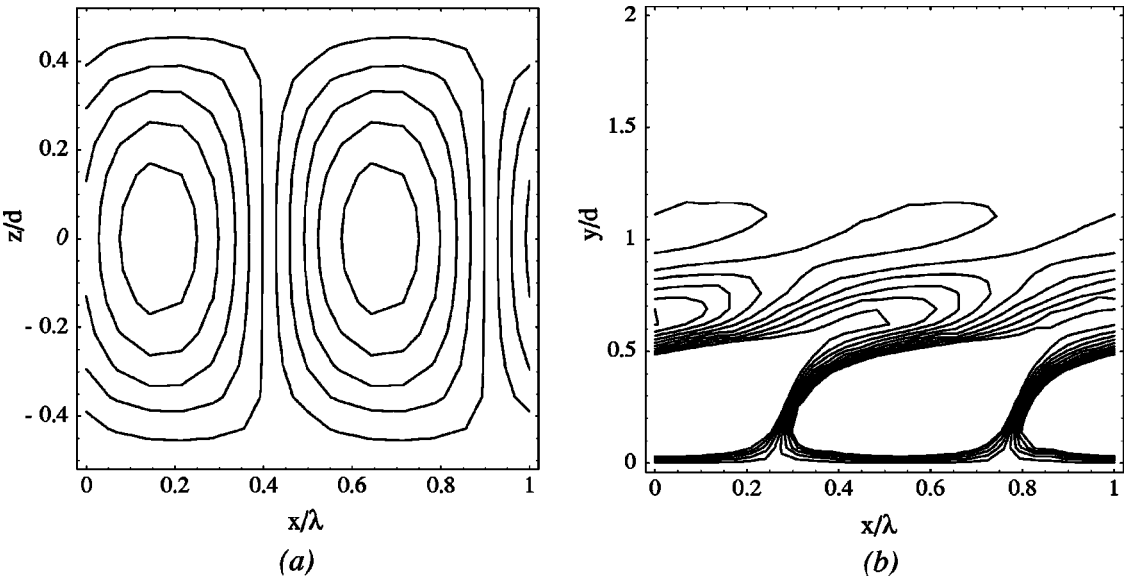

FIG. 2. Contourlines of (*a*) Re$[\overline{\phi^y}(z)\exp(ikx)]$ and (*b*) Re$[\overline{\psi^z}(y)\exp(ikx)]$ for $Ra=Ra_c$ and $\Omega=274$ with no-slip boundary condition, where $\overline{\phi^y}(z)$ and $\overline{\psi^z}(y)$ represent the average of ϕ over y and ψ over z, respectively.

and other numerical (GMNK,KC,HB) data where all the data are made dimensionless by scaling length by d, time by d^2/ν, and velocity by ν/d. In several cases the experimental data are sparse or have substantial error bars indicating a need for better data but we present the results of our numerical computation for the time when better data are available. We organize the presentation of the data in the following manner: First, we discuss the basic linear stability parameters Ra_c, k_c, and ω_c as functions of Ω. We then present coefficients for the CGL expansion, see Eq. (16), which include the marginal stability boundary curvature ξ_0, the linear group velocity v_g, the time scale τ_0, and the combination of complex coefficients c_0-c_1 which is measured in the experiments of NE and LE. Finally, we compare the experimentally obtained radial structure of the wall mode with a numerically computed linear eigenmode.

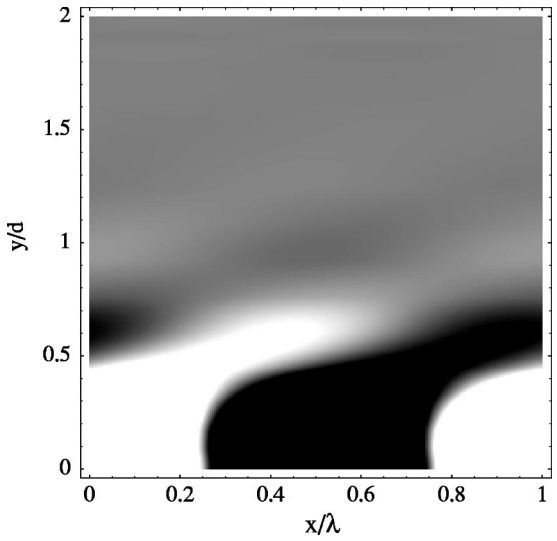

FIG. 3. Density plot of Re$[\overline{\theta^z}(y)\exp(ikx)]$ for $Ra=Ra_c$ and $\Omega=274$ with no-slip boundary condition, where $\overline{\theta^z}$ represents the average of θ over z.

We first compare our results for linear parameters Ra_c, k_c, and ω_c with the numerical results of GMNK, KC, and HB for free-slip top and bottom boundary conditions and with the experimental results of NE and LE. This comparison allows us to evaluate the importance of incorporating no-slip boundary conditions on the top and bottom and to estimate the influences of wall conductivity and wall curvature. In all the plots comparing experimental and numerical results, we use data points for experimental measurements and solid (no slip) or dashed (free slip) lines for the numerical results. In Fig. 4, experimental results for the critical Rayleigh number Ra_c for $\Gamma=5$ [17] are compared with numerical computations. Our free-slip calculations agree well with those of HB and show little difference for free-slip and no-slip top/bottom boundary conditions. The calculations of KC are slightly higher than the experimental values, whereas the calculations in finite geometry of GMNK are somewhat smaller. The KC results take into account the finite sidewall conductivity of the cell used by NE but the convection cell of LE had higher sidewall conductivity because of different cell construction. We have not conducted detailed calculations of this effect but it seems to be a reasonable explanation for remaining discrepancies between theory and experiment. Nevertheless, the agreement among the numerical results is excellent except for the finite aspect-ratio calculations of GMNK suggesting that small Γ lowers Ra_c slightly.

The effect of rigid top/bottom boundaries is more pronounced on the wave number. In Fig. 5, one sees again that the three calculations of k_c for free-slip top/bottom boundary conditions agree well. The no-slip boundary condition increases k_c by about 10% and nearly halves the difference between experiment and theory. The remaining discrepancy is unresolved as there is little apparent difference between the perfectly insulating calculations and the finite conductivity calculations of KC for the free-slip boundary condition. It

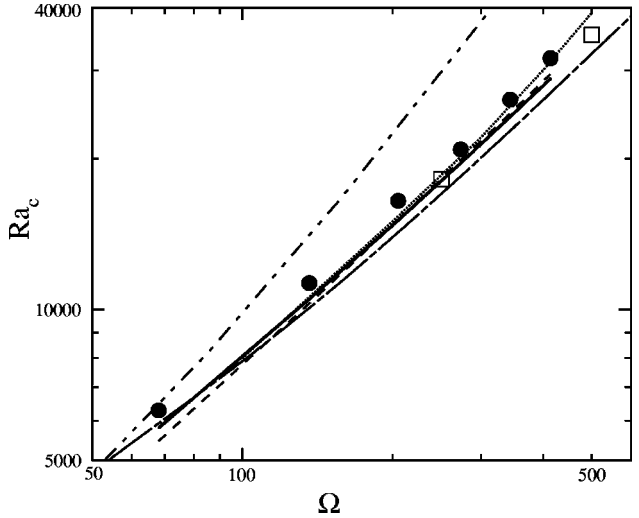

FIG. 4. Critical Rayleigh number Ra_c vs Ω for experimental data with Γ=5 (LE, solid circle), (HB, open square), Chandrasekhar 1961 (long-short-short dashed), (GMNK, long-short dashed), (KC, dotted line), free-slip top/bottom boundary conditions (dashed line), and no-slip top/bottom boundary conditions (solid line).

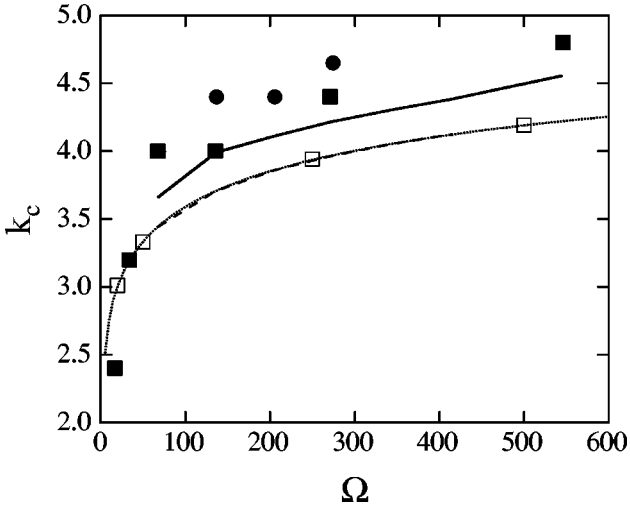

FIG. 5. Critical wave number k_c vs Ω for experimental data with Γ=5 (LE, solid circle), and Γ=2.5 by (NE, solid square), (HB, open square), (KC, dotted line), free-slip top/bottom boundary conditions (dashed line), and no-slip top/bottom boundary conditions (solid line).

is important to recall, however, that the periodic boundary conditions in the experiments lead to a discretization of k which is not reflected in the analysis, where use of an infinite x-domain makes k range over all the reals.

The largest change brought about by the use of realistic top/bottom boundary conditions is in the critical Hopf frequency. In Fig. 6, the three free-slip results are indistinguishable but are significantly above the experimental values. The rigid boundary conditions, however, yield excellent agreement with the experimental results. Again small sidewall conductivity does not seem to be important in the dependence of ω_c although in the high-conductivity limit there are substantial differences in all the critical parameters [5,9]. Another way to compare the calculations of the linear parameters is to consider ω_c as a function of k_c as illustrated in Fig. 7. The conclusion is that the main linear parameters agree reasonably well with experimental results and that the rigid top/bottom corrections improve the agreement.

Recently, two other calculations [12,13] were performed at Ω=274 that provide a check at that particular value for our linear stability calculations. The first was the same linear stability calculation as we performed with rigid top and bottom boundary conditions and a straight sidewall boundary [12]. The second was a direct numerical simulation of an annular geometry [13] in which the outer-sidewall and inner-sidewall states are only weakly coupled near onset and thus the calculated parameters should be a close approximation to the outer-sidewall state in a cylinder. In Table III, we compare the linear parameters obtained with Ω=274 for the experimental results of LE, the linear stability results of KC and P, the direct numerical simulation of SPCF, and our work. Our results agree perfectly with those of Plaut and are quite close to the results of the numerical simulations of SPCF. The largest difference is for v_g which we discuss in more detail below.

We now consider linear parameters that are related to the CGL expansion near onset and which are more difficult to measure precisely: the marginal stability boundary and the linear group velocity. In Fig. 8, we show the marginal stability boundary from our calculations and from the experiment by LE. Similar to the dependence of k_c on the boundary conditions, there is improvement in the agreement between experiment and theory using the rigid boundary conditions. The remaining differences are, however, outside the uncertainties of measurement. Finite sidewall conductivity could have an impact here. Another way to check the correspondence of the calculations and the experiment is to compare the stability boundaries as a function of Ω or, equivalently, ξ_0 for varying Ω. From Eq. (20), since we can fit the marginal stability boundaries to a parabola, we find the quadratic coefficient ξ_0 from the experimental data, as shown in Fig. 9.

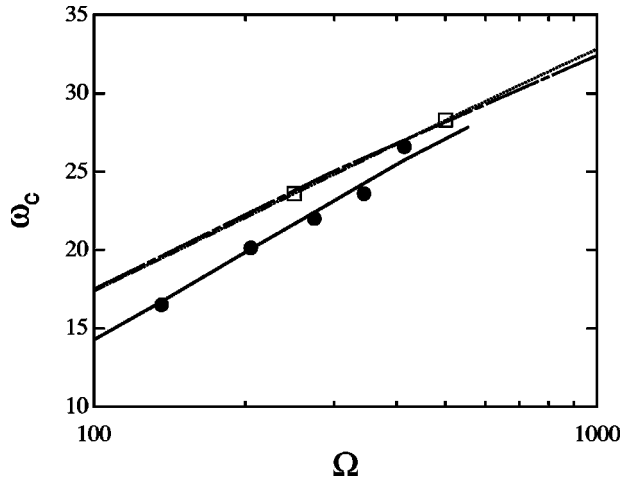

FIG. 6. Critical frequency ω_c vs Ω for experimental data with Γ=5 (LE, solid circle), (GMNK, long-short dashed), (KC, dotted line), (HB, open square), free-slip top/bottom boundary conditions (dashed line), and no-slip top/bottom boundary conditions (solid line).

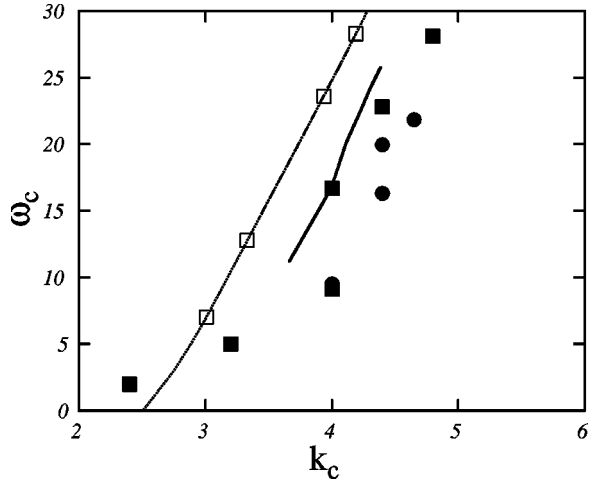

FIG. 7. Critical frequency ω_c vs k_c for experimental data with $\Gamma=5$ (LE, solid circle), and $\Gamma=2.5$ by (NE, solid square), (HB, open square), (KC, dotted line), free-slip top/bottom boundary conditions (dashed line), and no-slip top/bottom boundary conditions (solid line).

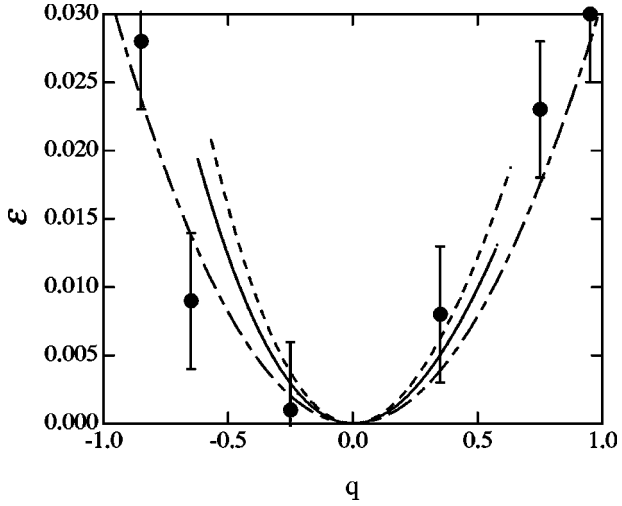

FIG. 8. Marginal stability boundary (ϵ_M vs q) for experimental data with $\Gamma=5$ (LE, solid circle), curve fit to the data (long-short dashed), free-slip top/bottom boundary conditions (dashed line), and no-slip top/bottom boundary conditions (solid line). $\Omega=274$.

The rigid boundary correction is in the right direction relative to the free-slip case but again does not fully account for the difference.

The comparison of the linear group velocity as a function of q is less satisfying but also the most difficult. The experimental determinations are made by extrapolating finite amplitude data to zero at the marginal stability boundary, which introduces some uncertainty. The higher-order corrections, i.e., quadratic in q, are even less robust because they are obtained [17] from phase dynamics near the center of the stability band. Thus, we compare our calculations with the experimental group velocity data only to linear order in q. In Fig. 10, the data and numerical results are compared. Our calculations of the linear group velocity as a function of q show some differences but in this case the use of rigid boundary conditions worsens rather than improves the agreement between experiment and theory. The slope of the linear dependence of v_g on q has the correct magnitude and does not change much with top/bottom conditions but the zero intercept becomes smaller when rigid conditions are included. The influence of curvature can be estimated from the difference between the linear stability calculation for a straight and thermally insulating sidewall where $v_g=1.9$, see Table III, and the direct numerical simulation of SPCF for a curved sidewall with insulating thermal boundary conditions where $v_g=2.0$. Thus, curvature seems to contribute less than a 5 % difference in v_g. The only remaining explanation is finite sidewall thermal conductivity. It is interesting to note that the results of Kuo [25] indicate that some quantities are not monotonic as a function of wall conductivity. This appears to be the case for v_g.

TABLE III. Comparison of linear coefficients of the rotating convection wall mode for $\Omega=274$ and $Pr=6.3$. Experiments are Liu and Ecke (LE) [17]. Linear stability calculations are Kuo and Cross (KC) [10], Plaut (P) [12], and our results. A direct numerical simulation by Scheel *et al.* (SPCF) is also included [13].

Source	Ra_c	k_c	ω_c	v_g	τ_0	ξ_0	$(c_0-c_1)/\tau_0$
LE	20850	4.65	−22.0	2.65	0.03	0.179	4.2
KC	19500	4.00	−24.0	2.22	0.026	0.24	14.4
P	19660	4.22	−22.4	1.91	0.025	0.21	6.4
SPCF	19500	4.2	−22.3	2.0	0.025	0.22	6.4
Present	19647	4.22	−22.4	1.92	0.025	0.21	6.4

Finally, we consider two quantities that have significant experimental uncertainties, but are sufficiently important to deserve a comparison with the numerical data. The characteristic time τ_0 and c_0-c_1 are plotted in Figs. 11 and 12 as a function of Ω. As is obvious from these plots, more experimental work is needed before a conclusion can be made regarding the effectiveness of including realistic top-bottom boundary condition. Notice that the no-slip dependence of

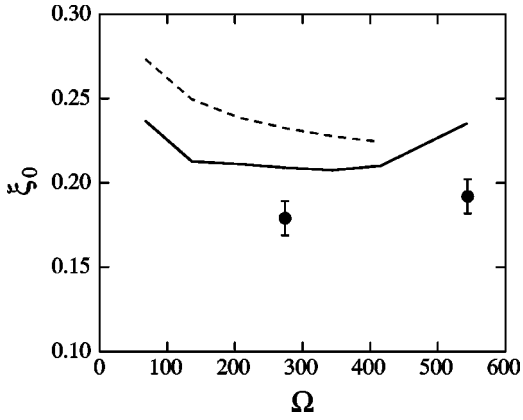

FIG. 9. Quadratic coefficient ξ_0 vs Ω from fit to marginal stability boundary. Experimental data with $\Gamma=5$ (LE, solid circle, $\Omega=274$) and $\Gamma=2.5$ (NE, solid circle, $\Omega=544$), free-slip top/bottom boundary conditions (dashed curve), and no-slip top/bottom boundary conditions (solid curve).

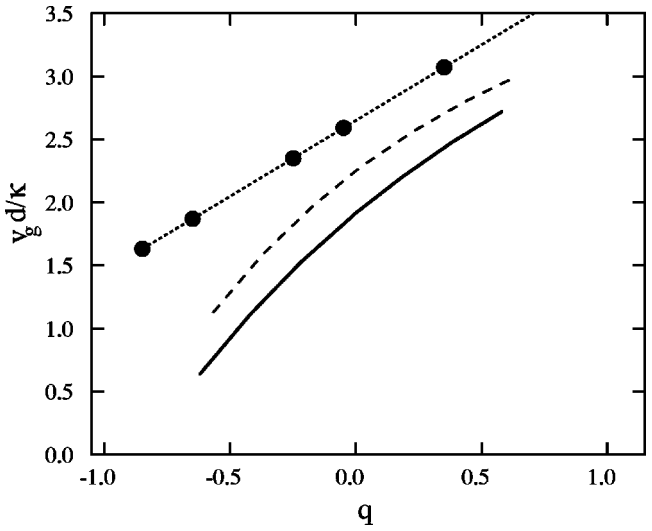

FIG. 10. Group velocity v_g vs q for experimental data with $\Gamma=5$ (LE, solid circle), curve fit to the data (dotted), free-slip top/bottom boundary conditions (dashed line), and no-slip top/bottom boundary conditions (solid line). $\Omega=274$.

c_0-c_1 on Ω indicates a trend that brings the no-slip curve closer to the free-slip curve for higher angular velocities Ω, but the free-slip curve seems closer to the experimental data point in this region.

Another comparison of interest is that of the radial structure of the experimental data with the computed linear eigenfunction for rigid top-bottom boundaries. In the experiment (LE), the shadowgraph intensity (proportional to temperature deviation from a linear profile) is computed over a narrow radial window by taking the standard deviation around the azimuthal direction. Uncertainties in the radial position are about 2 % near the wall and the determination of the intensity near the wall is difficult owing to light reflection from the boundary. The difficulties in this comparison are exacerbated by the finite amplitude of the data compared with the linear conditions of the eigenfunction which was calculated as closely as possible to match the experimental quantity. In

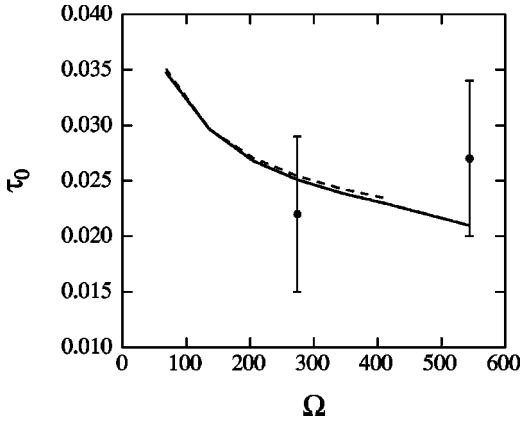

FIG. 11. Characteristic time τ_0 vs Ω for experimental data with $\Gamma=5$ (LE, solid circle, $\Omega=274$) and $\Gamma=2.5$ (NE) (solid circle, $\Omega=544$), free-slip top/bottom boundary conditions (dashed line), and no-slip top/bottom boundary conditions (solid line).

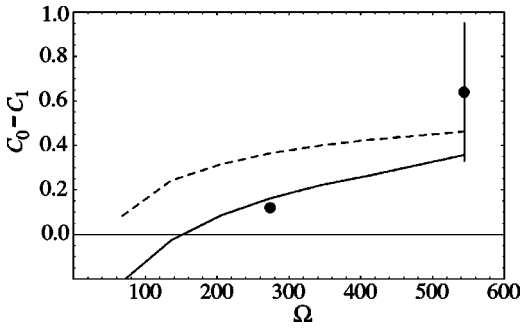

FIG. 12. c_0-c_1 vs Ω for experimental data with $\Gamma=5$ (LE) (solid circle, $\Omega=274$) and $\Gamma=2.5$ (NE) (solid circle, $\Omega=544$), free-slip top/bottom boundary conditions (dashed line), and no-slip top/bottom boundary conditions (solid line).

Fig. 13, we compare several data sets and the computed eigenfunction. We have made some small shifts in amplitude and radial position to obtain reasonable alignment. This is not a well-defined operation and thus the results should be viewed with caution. The clearest comparison is in the location and magnitude of the secondary peak in the temperature distribution. The location appears to be correct but the magnitude of this peak is considerably smaller in the computed eigenfunction.

IV. CONCLUSION

The inclusion of rigid top and bottom boundary conditions to the problem of the stability of traveling waves in rotating Rayleigh-Bénard convection for an infinite slab improves the agreement between theory and experiment. The critical Rayleigh number Ra_c is rather insensitive to the change in top/bottom boundary conditions. The slightly higher values of Ra_c for the experiments with $\Gamma=5$ suggest that the finite thermal conductivity of the sidewalls elevates Ra_c; recall that Ra_c for perfect conducting boundaries is close to the bulk linear onset at significantly higher values of Ra. The most dramatic improvement using the realistic top/bottom boundary conditions is in the variation of the critical frequency ω_c with Ω which now agrees very well with experiment. The critical wave number k_c dependence on Ω is

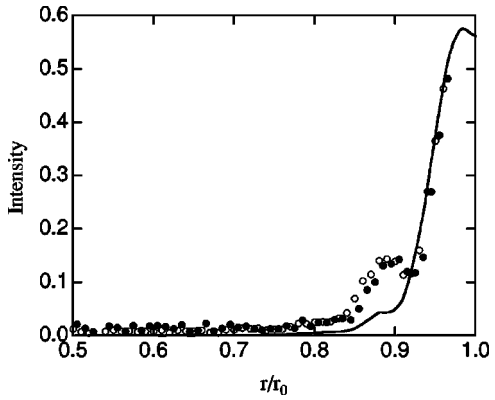

FIG. 13. Comparison of eigenfunctions between experiment (symbols) and numerical solution (solid line).

also improved by the new calculations but some difference remains. Similarly, the stability boundaries as a function of modulation wave number q are brought into closer, but not excellent, agreement with experiment for the realistic boundary conditions.

The source of the remaining differences between experiment and the results reported here may be attributed to finite sidewall conductivity in the experiments as opposed to the perfectly insulating boundary conditions used in the analysis. It would be useful in that regard to consider a single value of Ω and systematically investigate the variation of parameters as a function of sidewall conductivity. The other possible source of discrepancy between numerics and experiment is the cylindrical geometry of the experimental container. This radial curvature could affect, for example, the structure of the eigenfunction by enhancing the magnitude of the secondary peak. The periodic conditions imposed on the wave by the experimental geometry might also lead to some systematic variations in the parameters. On the other hand, a close comparison between the linear stability results at $\Omega = 274$ for a flat wall [12] and direct numerical simulations at the same Ω value for an annular geometry show little dependence on curvature for the main linear parameters.

ACKNOWLEDGMENTS

We acknowledge useful discussions with Hermann Riecke and Edgar Knobloch. This work was funded by the U.S. Department of Energy (Grant No. W-7405-ENG-36).

[1] S. Chandresekhar, *Hydrodynamic and Hydromagnetic Stability* (Oxford University Press, Oxford, 1961).
[2] T. Rossby, J. Fluid Mech. **36**, 309 (1969).
[3] V. P. Lucas, J. M. Pfotenhauer, and R. Donnelly, J. Fluid Mech. **129**, 251 (1983).
[4] J. M. Pfotenhauer, J. Niemela, and R. Donnelly, J. Fluid Mech. **175**, 85 (1987).
[5] J. C. Buell and I. Catton, Phys. Fluids **26**, 892 (1987).
[6] F. Zhong, R. E. Ecke, and V. Steinberg, Phys. Rev. Lett. **67**, 2473 (1991).
[7] F. Zhong, R. E. Ecke, and V. Steinberg, J. Fluid Mech. **249**, 135 (1993).
[8] R. E. Ecke, F. Zhong, and E. Knobloch, Europhys. Lett. **19**, 177 (1992).
[9] H. F. Goldstein, E. K. Knobloch, E. K. Mercader, and M. Net, J. Fluid Mech. **248**, 583 (1993).
[10] E. Y. Kuo and M. C. Cross, Phys. Rev. E **47**, R2245 (1993).
[11] J. Hermann and F. H. Busse, J. Fluid Mech. **255**, 183 (1993).
[12] E. Plaut, Phys. Rev. E **67**, 046303 (2003).
[13] J. D. Scheel, M. R. Paul, M. C. Cross, and P. F. Fisher, Phys. Rev. E **68**, 066216 (2003).
[14] L. Ning and R. E. Ecke, Phys. Rev. E **47**, 3326 (1993).
[15] M. C. Cross and P. C. Hohenberg, Rev. Mod. Phys. **65**, 851 (1993).
[16] Y. Liu and R. E. Ecke, Phys. Rev. Lett. **78**, 4391 (1997).
[17] Y. Liu and R. E. Ecke, Phys. Rev. E **59**, 4091 (1999).
[18] V. Eckhaus, *Studies in Nonlinear Stability Theory* (Springer-Verlag, Berlin, 1965).
[19] T. B. Benjamin and J. E. Feir, J. Fluid Mech. **27**, 417 (1967).
[20] A. Newell, *Envelope Equations*, Lectures in Applied Mathematics Vol. 15 (American Mathematical Society, Providence, RI, 1974).
[21] B. Janiaud, A. Pumir, D. Bensimon, V. Croquette, H. Richter, and L. Kramer, Physica D **55**, 269 (1992).
[22] Y. C. Hu, R. E. Ecke, and G. Ahlers, Phys. Rev. E **55**, 6928 (1997).
[23] F. Marques, M. Net, J. M. Massaguer, and I Mercader, Comput. Methods Appl. Mech. Eng. **110**, 157 (1993).
[24] P. G. Drazin and W. H. Reid, *Hydrodynamic Stability* (Cambridge University Press, Cambridge, 1981).
[25] E. Y. Kuo, Ph.D. thesis, Caltech, 1994.